

# HyPHEN: A Hybrid Packing Method and Optimizations for Homomorphic Encryption-Based Neural Networks

Donghwan Kim\*, Jaiyoung Park\*, Jongmin Kim, Sangpyo Kim, and Jung Ho Ahn

Seoul National University

{dhkim, jypark}@scale.snu.ac.kr

{jongmin.kim, vnb987, gajh}@snu.ac.kr

**Abstract**—Convolutional neural network (CNN) inference using fully homomorphic encryption (FHE) is a promising private inference (PI) solution due to the capability of FHE that enables offloading the whole computation process to the server while protecting the privacy of sensitive user data. However, prior FHE-based CNN (HCNN) implementations are far from being practical due to the high computational and memory overheads of FHE. To overcome this limitation, we present HyPHEN, a deep HCNN construction that features an efficient FHE convolution algorithm, data packing methods (hybrid packing and image slicing), and FHE-specific optimizations. Such enhancements enable HyPHEN to substantially reduce the memory footprint and the number of expensive homomorphic operations, such as ciphertext rotation and bootstrapping. As a result, HyPHEN brings the latency of HCNN CIFAR-10 inference down to a practical level at 1.40s (ResNet20) and demonstrates HCNN ImageNet inference for the first time at 16.87s (ResNet18).

**Index Terms**—Private Inference, Fully Homomorphic Encryption

## I. INTRODUCTION

Private inference (PI) has recently gained the spotlight in the MLaaS domain as cloud companies should comply with privacy regulations such as GDPR Regulation [1] and HIPAA Act [2]. PI enables inference services at the cloud server while protecting the privacy of the client and the intellectual properties of the service provider. For instance, hospitals can provide a private medical diagnosis of diseases, and security companies can provide private surveillance systems without accessing client’s sensitive data [3], [4].

Fully homomorphic encryption (FHE) [5] is a cryptographic primitive that enables direct evaluation of a rich set of functions on encrypted data, making it especially suited for PI among other cryptographic candidates [6], [7]. FHE-based PI solution uniquely features 1) full offloading of the computation process to the server, 2) succinct data communication requirement, and 3) non-disclosure of any information about the model except the inference result. Such benefits have driven researchers to investigate FHE-based PI of convolutional neural networks (HCNN) [8]–[12].

However, FHE incurs high computational and memory overheads, hindering the adoption of HCNN for real-world services. Several prior works has tried to mitigate the overheads [11], [13], but HCNN implementations still stay at a proof-of-concept

level and target elementary problems such as MNIST and CIFAR-10. Gazelle [14] proposes a convolution algorithm for homomorphic encryption, which is widely adopted and by the following studies [11], [15], [16]. Gazelle and most prior PI CNN implementations have avoided the high overheads of FHE by restricting the CNN models to shallow ones [8], or mixing use of other cryptographic primitives, such as multi-party computation (MPC) [15], [17], [18]; however, MPC solutions require extra user intervention and the associated data communication overheads. The state-of-the-art FHE solution [11] modifies Gazelle’s algorithm by densely mapping data into a ciphertext before entering the next convolution layer, and optimizes it for FHE circumstances. Despite such efforts, prior implementations take tens of minutes [11] to even hours [13] to perform a single HCNN inference of CIFAR-10 (ResNet20).

We propose HyPHEN, which mitigates the huge overhead of HCNN with an optimized convolution algorithm and packing methods. We observe that, in HCNN, rotation operations take up the majority of the runtime (see Appendix A). Most of the rotations are performed to maintain the data organization inside an encrypted tensor uniformly throughout HCNN inference. *Lazy-SISO* algorithm and *hybrid packing (HP)* method of HyPHEN allow switching between multiple data organizations to get rid of excessive rotation operations. Also, our *image slicing* method tackles the data expansion problem of HCNN by enhancing data reuse with only 2.5% runtime computational overhead, and saves hundreds of GBs of memory space. By these means, our GPU implementation of HyPHEN achieves 1.40s of execution time for encrypted CIFAR-10 inference with the ResNet20 model, reaching a real-time level. Also, HyPHEN shows HCNN inference for ImageNet inference with the ResNet18 model for the first time, which takes 16.87s. The key contributions of the paper are as follows:

- We devise an optimized algorithm for convolution, which alternates between two methods, *channel-aligned convolution (CAConv)* and *replication-aligned convolution (RAConv)*, where such composition is enabled by our novel lazy-SISO algorithm.
- We propose a *hybrid packing (HP)* method that can utilize the entire slots of a ciphertext with a marginal increase in the number of rotations.

- We show the huge memory footprint of HCNN deteriorates its performance and propose an *image slicing* method that can save hundreds of GBs of memory space with negligible overhead.

## II. BACKGROUND

### A. Fully Homomorphic Encryption (FHE)

FHE is a set of public key encryption schemes that enable computation on encrypted data. Among several popular FHE schemes, RNS-CKKS [19] has been broadly adopted in the PI domain as it supports fixed-point numbers and *slot batching*. A *plaintext* in RNS-CKKS is an unencrypted degree- $(N-1)$  polynomial in a cyclotomic polynomial ring,  $R_Q = \mathbb{Z}_Q[X]/(X^N+1)$ . A plaintext maps to a message which is a vector of  $N/2$  real (or complex) numbers, i.e., a single plaintext batches  $N/2$  slots, each of which can store a complex or real number. CKKS encrypts a plaintext into a *ciphertext* in  $R_Q^2$ .  $Q$  is a ring modulus represented by a set of prime moduli obtained by the Chinese Remainder Theorem (CRT) as  $Q = \prod_{i=0}^l q_i$  ( $0 \leq l \leq L$ ).  $L$  and  $l$  denote the initial and current *level* of a ciphertext, which is an HE-specific resource that determines the number of multiplications applicable to a given ciphertext. We also denote the associated level of ring modulus using subscript as  $Q_L$  or  $Q_l$ . We denote the plaintext and ciphertext of a message  $\mathbf{a}$  as  $\langle \mathbf{a} \rangle$  and  $[\mathbf{a}]$ . HE operations of addition, multiplication, and rotation can be described as follows:

- $\text{HE.Eval}([\mathbf{a}], [\mathbf{b}], f_l) = \text{HE.Eval}(\langle \mathbf{a} \rangle, \langle \mathbf{b} \rangle, f_l) = [f_l(\mathbf{a}, \mathbf{b})]$
- $\text{HE.Rotate}([\mathbf{a}], r) = [\text{rot}(\mathbf{a}, r)]$

$f_l$  denotes linear operations, either addition or (Hadamard) multiplication.  $\text{rot}(\mathbf{a}, r)$  represents cyclically shifting vector  $\mathbf{a}$  by  $r$  to the left. Unlike addition and rotation, multiplication in RNS-CKKS requires additional rescale operation, which consumes a level by dividing  $ct \in R_{Q_l}$  into  $ct' \in R_{Q_{l-1}}$ . If a ciphertext has no level left after a series of multiplications, *bootstrapping* [20] is needed to reconcile the levels and allow further operation. Bootstrapping, the most costly operation in HE, consists of multiple HE operations including rescale operations. After bootstrapping, the level of the resulting ciphertext becomes  $L' = (L - L_b)$  where  $L_b$  is the depth of rescale operations in the bootstrapping circuit. As it is beneficial to perform many operations before bootstrapping,  $L$  should be sufficiently larger than  $L_b$ . However, large  $L$  decreases the *security level*, which should be high enough to tolerate cryptographic attacks. The security level is roughly proportional to  $N/L$ . Considering the security requirement of HE, large  $L$  requires large  $N$  ( $\geq 2^{15}$ ). Thus, prior works on FHE [21]–[23] target  $N = 2^{15}$  to  $2^{17}$ .

Table I shows the execution time of HE operations on a system specified in Section IV-A. We measured the execution time of each operation at the initial level ( $L'$ ) of a ciphertext and thus the execution time may decrease for ciphertexts with lower levels. Bootstrapping consumes over two orders of magnitude longer runtime than other operations, but bootstrapping does not occur as frequently as others. Except for bootstrapping, Rotate and MulCt are the most time-consuming operations in HE, which is due to the expensive key-switching procedure.

TABLE I: Benchmark of HE operations averaged over 100 iterations on CPU (64 threads). Pt and Ct postfixes each represents ciphertext-plaintext and ciphertext-ciphertext operation, respectively.

Operation	AddPt	AddCt	MulPt	MulCt	Rescale	Rotate	Boot
Time (ms)	0.572	0.202	0.506	17.3	3.90	15.5	2160

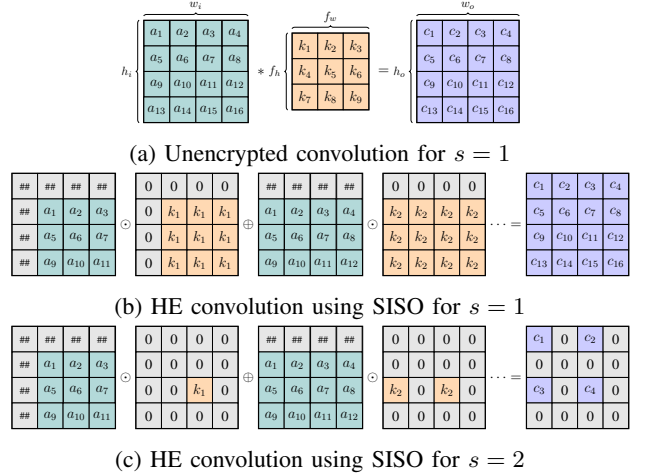


Fig. 1: Single-input and single-output channel convolution (SISO). Ciphertexts and plaintexts are illustrated as 2D matrices, but are actually stored in 1D manner with each matrix row concatenated.

### B. Convolution on Homomorphic Encryption

In this subsection, we describe the baseline HCNN algorithms. We represent input and output tensors with tuples  $\{w_i, h_i, c_i\}$  and  $\{w_o, h_o, c_o\}$ , and convolution layers with  $\{f_w, f_h, c_i, c_o\}$ . We denote the stride of convolution as  $s$  and assume *padding* = 1 for simplicity.

**Single-input, single-output channel convolution (SISO):** Gazelle [14] proposes efficient convolution algorithms on HE, referred to as SISO. Figure 1 shows SISO for  $s = 1, 2$ . Filter elements are separated into  $f_w, f_h$  plaintexts. Each slot in  $i$ -th plaintext stores  $k_i$  or 0 (punctured) depending on whether  $k_i$  is involved in the computation of the output pixel at the same slot. SISO operates as follows: 1) rotate an encrypted input image with different indexes according to plaintext filter, 2) perform multiplication, and 3) accumulate the multiplication results to obtain the output.

**Channel-aligned convolution (CAConv):** For multiple channels, convolution is performed in a SIMD manner. If the size of a channel ( $w_i h_i$  or  $w_o h_o$ ) is smaller than the number of slots in a ciphertext, multiple channels can be placed in a ciphertext. For example, if  $slot = 2^{15}$  and an input channel is sized  $w_i h_i = 32 \times 32$  as in the input image of the CIFAR-10 dataset,  $\frac{slot}{w_i h_i} = 32$  channels can be placed in a single ciphertext in an aligned manner (i.e., *channel-aligned*). Suppose we perform convolution on a channel-aligned input ciphertext with  $c_i = \frac{slot}{w_i h_i}$  channels. First, SISO is performed on  $c_i$  input

channels in a SIMD manner (see Figure 2a), which produces  $c_i c_o$  convolution outputs  $MK^{(i,j)}$  ( $1 \leq i \leq c_i, 1 \leq j \leq c_o$ ). To compute the result for the  $k$ -th output channel,  $\sum_{i=1}^{c_i} MK^{(i,k)}$  is accumulated by *RaS* (*Rotate and Sum*). *RaS* is repeated for each of  $c_o$  output channels. Throughout this paper, we refer to this convolution that takes a channel-aligned ciphertext as the input as *channel-aligned convolution* (*CACConv*).

**Input repetition:** *CACConv* can be further optimized when the input tensor is smaller than the number of slots in a ciphertext.  $\frac{\text{slot}}{w_i h_i c_i}$  copies of the input tensor can be placed in a ciphertext, then  $\frac{\text{slot}}{w_i h_i c_i}$  output channels can be computed together with a single input ciphertext [11].

**Replication-aligned convolution (RAConv):** The output ciphertexts of *CACConv* holds multiple replications of a single output channel (i.e., *replication-aligned*). To perform another convolution, additional operations are required to realign the ciphertexts into the channel-aligned form, which we refer to as *IR* (*Image Realignment*). [12] constructs a framework supporting a broad scope of convolution algorithms for ciphertexts with various alignments. We build on the framework and design *replication-aligned convolution* (*RAConv*). In *RAConv*, each replication-aligned ciphertext is multiplied with plaintexts containing filter weights for different output channels, whose results can be accumulated to produce a single channel-aligned ciphertext (see Figure 2b). Therefore, *CACConv* and *RAConv* can be performed in an alternative manner to get rid of costly *IR* computation, when performing multiple convolutions.

**Packing:** Strided convolution ( $s > 1$ ) using *SISO* creates a gap between valid values (see Figure 1c). A ciphertext with a gap underutilizes its slots, leading to throughput degradation. While *Gazelle* removes the gap by a client-aided re-encryption process, non-interactive *PI* should remove the gap through masking and rotation, which incur additional computation and level consumption. [11] propose a *multiplexed packing* method that can be combined with *CACConv* (*MP-CACConv*) to mitigate the overheads. In the *IR* stage of *MP-CACConv*, the gap is filled with other channels (see Figure 3b), which we refer to as the *repacking process*. Therefore, *IR* incorporates both realigning and repacking processes in *MP-CACConv*.

There are many variants of the convolution algorithm for HE [11], [13], [15], [16], [24], but most of them resort to *SISO*. [12] devise a convolution algorithm based on tile tensoring, and not *SISO*, which can be an efficient alternative to *SISO* for specific HE parameter settings and image sizes. However, we find that tile tensoring incurs an excessive amount of bootstrapping for FHE circumstances in general, so we exclude it from analysis and mainly focus on *SISO* convolution in the paper.

### C. Activation Function on Homomorphic Encryption

Non-linear activation functions, such as ReLU, cannot be used directly in HCNN. They must be replaced by polynomial functions as HE only supports addition and multiplication operations. Direct replacement of non-linear functions with approximate polynomials requires the approximation error to be kept low over a wide range, to retain the accuracy

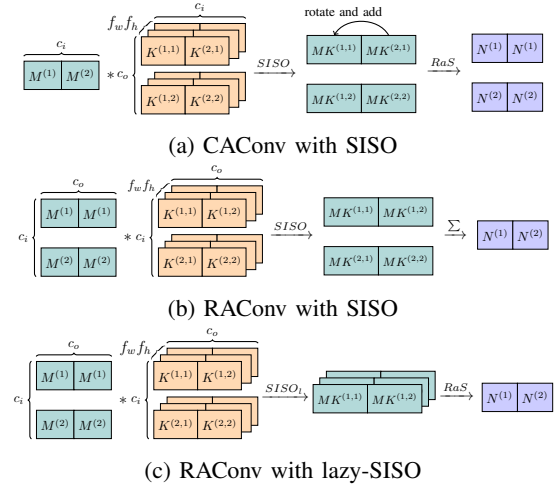


Fig. 2: *CACConv* and *RAConv*. The single superscript denotes channel and the superscript pair denotes (input channel, output channel). We simplify the notation of  $M^{(a)} K^{(a,b)}$  as  $MK^{(a,b)}$ .

$a_1^{(1)}$	0	$a_2^{(1)}$	0
0	0	0	0
$a_3^{(1)}$	0	$a_4^{(1)}$	0
0	0	0	0

(a) Void packing

$a_1^{(1)}$	$a_1^{(2)}$	$a_2^{(1)}$	$a_2^{(2)}$
$a_1^{(3)}$	$a_1^{(4)}$	$a_2^{(3)}$	$a_2^{(4)}$
$a_3^{(1)}$	$a_3^{(2)}$	$a_4^{(1)}$	$a_4^{(2)}$
$a_3^{(3)}$	$a_3^{(4)}$	$a_4^{(3)}$	$a_4^{(4)}$

(b) Multiplex packing

$a_1^{(1)}$	$a_1^{(1)}$	$a_2^{(1)}$	$a_2^{(1)}$
$a_1^{(1)}$	$a_1^{(1)}$	$a_2^{(1)}$	$a_2^{(1)}$
$a_3^{(1)}$	$a_3^{(1)}$	$a_4^{(1)}$	$a_4^{(1)}$
$a_3^{(1)}$	$a_3^{(1)}$	$a_4^{(1)}$	$a_4^{(1)}$

(c) Duplicate packing

$a_1^{(1)}$	$a_1^{(2)}$	$a_2^{(1)}$	$a_2^{(2)}$
$a_1^{(1)}$	$a_1^{(2)}$	$a_2^{(1)}$	$a_2^{(2)}$
$a_3^{(1)}$	$a_3^{(2)}$	$a_4^{(1)}$	$a_4^{(2)}$
$a_3^{(1)}$	$a_3^{(2)}$	$a_4^{(1)}$	$a_4^{(2)}$

(d) Hybrid packing

Fig. 3: Comparison of gap packing methods to fill gap induced by downsampling layers.  $a_i^{(j)}$  denotes the  $i$ -th element in the  $j$ -th channel of a tensor  $a$ .

of a CNN model. [25] approximate ReLU while keeping  $l_1$  norm of approximation error lower than  $2^{-13}$  in the range of  $[-50, 50]$ , using a composition of 15-, 15-, and 27-degree polynomials. Approximation-based approach has a benefit that it can be applied to pre-trained neural networks. However, evaluation of high-degree polynomials imposes a significant runtime overhead in HCNN inference.

Another approach is to train neural networks with low-degree polynomial activation functions as in [26]–[30]. While this approach requires retraining, operational cost is much cheaper compared to high-degree polynomials. Recently, AESPA [31] has demonstrated that CNN trained with low-degree polynomials can achieve equivalent accuracy to ReLU-based networks across various CNN networks and image datasets. AESPA replaces ReLU and batch normalization (BN) with the

composition of orthogonal basis polynomials and basis-wise BN. During inference, the composition turns into a second-degree polynomial, so AESPA can drastically reduce runtime cost for activation. Therefore, we adopt AESPA for our HCNN implementation.

#### D. Threat Model

We adopt the same threat model as prior PI works on HE [8], [11]. A client sends encrypted data to an untrusted server. The server performs CNN inference using HE operations and returns inference results to the client. The client decrypts the resulting ciphertext to obtain the private result. The server only holds the client’s public keys and cannot decrypt any intermediate ciphertexts in the inference process. The client does not know any information about the processing at the server other than the result.

### III. HYPHEN CONSTRUCTION

We introduce HyPHEN, our HCNN solution which focuses on reducing the memory footprint and the number of expensive homomorphic operations, including rotation and bootstrapping. We implement ResNet [32] models for CIFAR-10 and ImageNet inference tasks with HyPHEN to demonstrate its effectiveness.

#### A. RACnv and Lazy-SISO

The main performance bottleneck of CACnv is the massive number of rotations. CACnv requires an enormous number of rotations for RaS and IR, which take up most of the time in CACnv. For example, rotations for RaS and IR respectively account for 49% and 43% of the total rotations in an MP-CACnv implementation of ResNet20. Furthermore, IR consumes an additional level for masking to extract the values. RACnv does not require RaS and reduces the overheads for IR when alternatively performed with CACnv, but it requires more rotations for SISO. While CACnv requires  $(f_w f_h - 1)$  rotations for SISO, RACnv requires  $(f_w f_h - 1)$  rotations for each of  $c_i$  input ciphertexts.

We devise lazy-SISO algorithm, which reduces the number of rotations for RACnv. With lazy-SISO, rotations are delayed to be performed after multiplications with weight plaintexts. Then, the accumulation step in RACnv transforms into an RaS step (see Figure 2c), which only requires  $(f_w f_h - 1)$  rotations. Without Lazy-SISO, simply alternating between CACnv and RACnv does not have much performance benefit due to additional SISO overheads. See Appendix A for more details of lazy-SISO.

#### B. Hybrid Packing

SISO convolution suffers from low slot utilization in ciphertexts due to the gap created by strided convolutions, which leads to severe throughput degradation in HCNN. Prior state-of-the-art HCNN implementation (MP-CACnv) mitigates the underutilization of slots by packing input ciphertexts as dense as possible using multiplexed packing and input repetition (see Section II-B). However, such dense packing causes a lot of additional rotations to adjust the data organization because

SISO still produces a void-packed ciphertext (see Figure 3a) even if the input ciphertext is densely packed. MP-CACnv has to manually restore the dense data organization by masking off invalid values and filling the gap with the values from different channels during the IR process. As a result, MP-CACnv ends up requiring additional  $c_o$  rotations to maintain multiplexed packing and  $\log \frac{\text{slot}}{w_o h_o c_o}$  rotations to maintain input repetition.

To reduce the repacking overhead between convolutional layers, we propose a novel *hybrid packing (HP)* method. HP fills the gap with duplicates of multiple channels (See Figure 3d). We design HP based on two key observations. First, applying convolution over a duplicate-packed ciphertext (Figure 3c) produces a multiplex-packed output ciphertext as in Figure 3b. Second, converting a void-packed ciphertext into a duplicate-packed ciphertext requires fewer rotations than converting it into a multiplex-packed ciphertext. Duplicate packing only needs  $O(\log(\text{gap}_{\text{size}}))$  rotations while multiplexed packing requires  $O(\text{gap}_{\text{size}})$  rotations.

We represent a hybrid-packed ciphertext by a pair of  $(m, d)$ , where  $m$  is the number of multiplexed channels, and  $d$  is the number of duplicates. For example, Figure 3d shows  $(m, d) = (2, 2)$  HP. Data organization for HP can differ even for the same  $(m, d)$  parameter, and depends on the convolution algorithm. HP parameter  $(m, d)$  changes when CACnv or RACnv is performed as shown in Figure 4. We denote  $(m, d)$  of the input and output ciphertexts as  $(m_{\text{in}}, d_{\text{in}})$  and  $(m_{\text{out}}, d_{\text{out}})$ . Input repetition is no longer required as HP with larger  $d_{\text{in}}$  can be used instead. During convolution, duplicates of the same element produce output elements in different channels ( $c^{(1)} - c^{(4)}$  in Figure 4a, and  $c^{(1)}$  and  $c^{(17)}$  in Figure 4b). Therefore, after the IR process, we get output ciphertexts with the HP parameter set to  $(m_{\text{out}}, d_{\text{out}}) = (d_{\text{in}}, m_{\text{in}})$ . So, after a series of CACnv and RACnv, the HP parameter returns to the initial  $(m_{\text{in}}, d_{\text{in}})$ . The complete procedures of RACnv and CACnv with HP are described more in detail in Appendix A.

Compared to MP-CACnv, HP significantly reduces the rotations in RaS and IR. The rotation counts of MP-CACnv [11] and our HP convolutions are shown in Table II. For both HP convolution methods, the product of the numbers of input and output ciphertexts remains constant ( $ct_{\text{in}} \cdot ct_{\text{out}} = \frac{w_i h_i c_i c_o}{\text{slot}}$ ). Compared to MP-CACnv, the number of rotations for RaS is reduced by about  $ct_{\text{in}}$  times for both HP-CACnv and HP-RACnv. Also, the number of rotations required for repacking decreases from  $c_o$  of MP-CACnv to mere  $\log m_{\text{in}}$  per output ciphertext in our HP convolutions. Although HP requires slightly more rotations for SISO ( $ct_{\text{min}}$  of HP convolutions are usually higher than  $ct_{\text{in}}$  of MP-CACnv), HP reduces the overall number of rotations required for convolution. We also explore various combinations for the  $(m, d)$  pair to minimize the total number of rotations. The choice of  $(m, d)$  decides  $ct_{\text{in}}$  and  $ct_{\text{out}}$  values and creates a trade-off between SISO, RaS, and IR costs, and also affects the number of ciphertexts we have to perform bootstrapping with. We provide an in-depth performance analysis with regard to the choice of  $(m, d)$  in Appendix A.

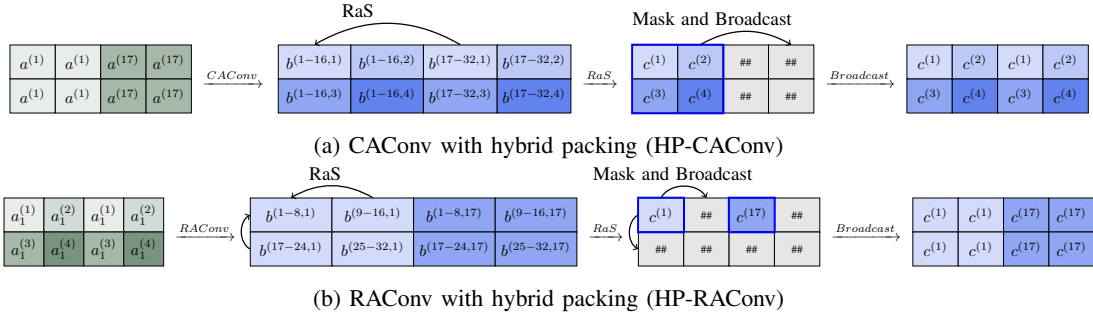
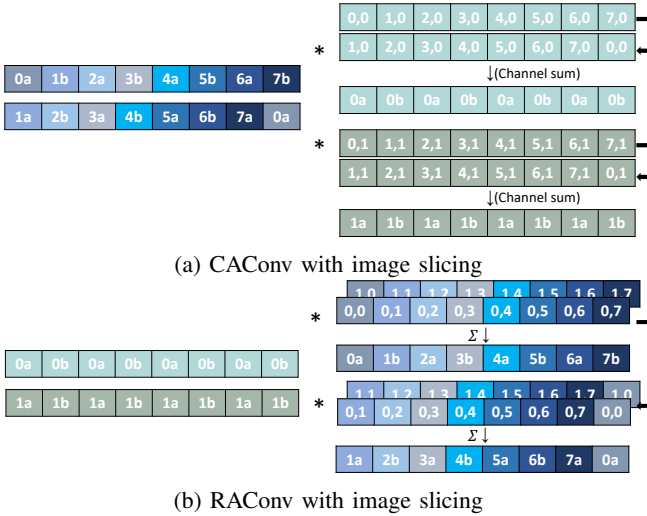


Fig. 4: The procedure of CAConv and RAConv with hybrid packing

TABLE II: The rotation complexity of the convolutions. We denote the numbers of input and output ciphertexts as  $ct_{in}, ct_{out}$ . Then,  $ct_{min} = \min(ct_{in}, ct_{out})$  considering SISO and lazy-SISO.

Method	$ct_{in}$	$ct_{out}$	SISO	RaS	IR
[11]	$\lceil \frac{w_i h_i c_i}{slot} \rceil$	$\lceil \frac{w_o h_o c_o}{slot} \rceil$	$ct_{in}(f_w f_h - 1)$	$\frac{w_i h_i c_i c_o}{slot} \log c_i$	$c_o + \log \frac{slot}{w_o h_o c_o}$
HP-CAConv	$\frac{w_i h_i c_i d_{in}}{slot}$	$\frac{c_o}{d_{in}}$	$ct_{min}(f_w f_h - 1)$	$ct_{out} \log \frac{c_i}{ct_{in}}$	$ct_{out} \log m_{in}$
HP-RAConv	$\frac{c_i}{m_{in}}$	$\frac{w_i h_i c_o m_{in}}{slot}$	$ct_{min}(f_w f_h - 1)$	$ct_{out} \log m_{in}$	$ct_{out} \log m_{in}$



(b) RAConv with image slicing

Fig. 5: Simplified convolution processes with image slicing. Ciphertexts are filled with image slices each represented with a channel number and a postfix: upper half of image as  $a$  and lower half as  $b$  (e.g.  $3b$  represents the lower half of the 3<sup>rd</sup> channel). Ciphertexts are multiplied with plaintexts holding weight values, where  $i, j$  on each slice represents weight values for  $i$ -th input channel, and  $j$ -th output channel. Black arrow represents plaintext permutation.

### C. Image Slicing

In HCNN inference, weight plaintexts take the majority of the memory footprint. In the ResNet models in our experiment, plaintexts take tens to hundreds of GBs of memory space, occupying the majority of the memory footprint. The plaintext packing method of SISO replicates each filter element  $w_i h_i$  times to form a weight plaintext (see Figure 1b), which requires

a total of  $w_i h_i f_w f_h c_i c_o$  plaintext slots for a weight tensor. Such plaintext data expansion increases the cost of HCNN inference in terms of storage capacity and memory bandwidth. For instance, plaintexts for running ResNet18 on ImageNet take up 379GB of memory space (see Table III), which even exceeds the memory capacity of the latest GPUs, limited by the current HBM technology.

We find a method to reduce data expansion of plaintexts, by organizing the weights in a circular way such that they can be permuted at runtime when being multiplied with the input ciphertexts. This results in a packing method for ciphertexts shown in Figure 5, which we refer to as *image slicing*. In CAConv, the input image is divided into  $s_i$  (2 in the figure) slices, and different slices are chosen from each channel to be placed in a single ciphertext. This organization enables each plaintext to be reused by  $s_i - 1$  permutations. After accumulation, the output ciphertext follows a simple replication-aligned organization. After modified RAConv with image slicing shown in Figure 5b, the organization returns to the image-sliced one.

Image slicing can be orthogonally applied along with HP, and reduce the memory footprint for plaintexts roughly by a factor of  $s_i$ . Extra computation of plaintext permutation during image-sliced convolution is not significant to the overall performance because plaintext permutation is much less complex than other homomorphic operations; plaintext permutation only involves moving data elements. We use  $s_i = 8$  for ImageNet implementations of HyPHEN, but do not apply image slicing to CIFAR-10. Image slicing requires an explicit zero padding inside a ciphertext, to which the small image size of CIFAR-10 (e.g.,  $16 \times 16$  space is required for a  $8 \times 8$  feature map) is not well suited. Zero padding overhead outweighs the benefit of image slicing, so it is not applied to CIFAR-10.

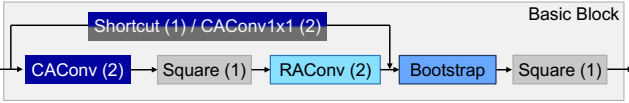


Fig. 6: ResNet basic block built on HyPHEN. The level consumption per block is written in parentheses. In the downsampling block, pointwise convolution is added to the critical path. Otherwise, a simple shortcut is added.

#### D. ResNet Construction with HyPHEN

HyPHEN combines RAConv, HP and Image Slicing to build the entire CNN model. Figure 6 shows the basic block of ResNet implemented on HyPHEN. There are three more considerations when deciding the order of operations. First, bootstrapping is cheaper when placed after RAConv, and not CAConv, because the number of ciphertexts is smaller for the former. Second, to match the level between the shortcut path and the main CAConv-RAConv path, bootstrapping should be placed either before residual connections diverge or after they converge. Last, it is beneficial to perform convolutional layers at the lowest level possible because the complexity of FHE operations such as rotation is proportional to the level  $l$  of the ciphertext.

All things put together, our ResNet basic block consumes a total of 6 levels. The level consumption of each layer is represented in the parenthesis of each block. CAConv and RAConv use HP and consume one level for each of SISO and IR. Activation uses AESPA and consumes one level. AESPA is a quadratic polynomial having different coefficients for each channel while training. During inference, we fuse the coefficients into nearby layers, then the activation becomes a simple square function  $x^2$ . We set the ciphertext level after bootstrapping ( $L'$  in Section II-A) to six and perform bootstrapping when the level becomes zero.

### IV. EVALUATION

#### A. Experimental Setup

We ran HCNN inference on CPU and GPU environments using the RNS-CKKS library, HEaAN [33]. The CPU system is equipped with two AMD EPYC 7452 CPUs running at 2.35GHz (32 cores per socket) and 480GB DRAM. GPU experiments were conducted at the same system with an additional NVIDIA A100 GPU with 80GB HBM. Our HCNN inference experiments used the CIFAR-10 [34] and ImageNet [35] datasets. We evaluated ResNet20/32/44/18 trained with AESPA on PyTorch and applied the fusion technique to all the networks. Our RNS-CKKS parameters satisfy 128-bit security level [36] with polynomial degree  $N = 2^{16}$  and hamming weight 192. The bootstrapping implementation consumes 17 levels.

#### B. Performance

We first compare HyPHEN against Cheetah [18], one of the state-of-the-art HE-MPC hybrid PI protocol. As it is hard to make a fair comparison between the HCNN and HE-MPC as the preferred system settings are different, we set out to

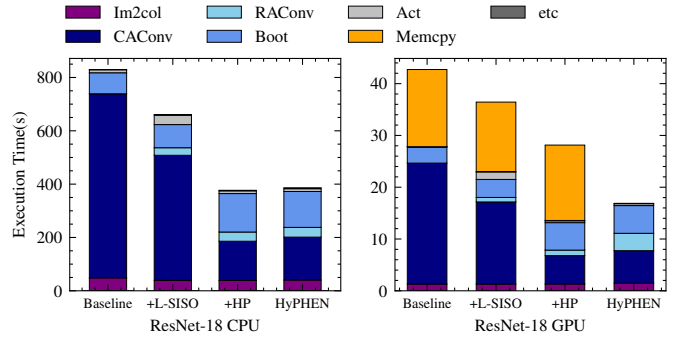


Fig. 7: HCNN inference time of ResNet18 (ImageNet) on our CPU and GPU systems.

TABLE III: Memory footprint of ResNet-18 on ImageNet. We extended the implementation of [11] to ImageNet and estimated the memory footprint. The baseline is [11] augmented with AESPA, where HyPHEN improves it with image slicing.

Implementation	Weight Plaintext (GB)	Eval key (GB)
[11]	275.4	137.4
Baseline	379.3	11.3
<b>HyPHEN</b>	47.0	11.3

use the best result presented in the paper. Here, HyPHEN is  $11.3\times$  faster than Cheetah on ResNet32 considering the end-to-end runtime and  $5.5\times$  efficient than Cheetah in terms of communication. Although the HE-MPC hybrid PI protocol is generally accepted as faster than HCNN, equipped with efficient packing scheme and hardware acceleration, we show that the performance of HCNN inference is comparable.

In FHE domain, [11], [13] has priorly shown ResNet on CIFAR-10, while [11] reported single thread implementation of ResNet20 in 2271s. HyPHEN shows significant latency reduction on image classification. Our work conduct the same task in 37.6 seconds in 64 thread CPU environment, and further reduces within 1.4 seconds in GPU.

#### C. Sensitivity Study

To analyze the effectiveness of each component of HyPHEN, we started from the HCNN implementation of [11] augmented with AESPA (Baseline), and gradually applied alternation between CAConv and RAConv with lazy-SISO (+ L-SISO), HP (+ HP), and image slicing (HyPHEN). We tested with CPU/GPU implementations of ResNet18 for ImageNet. The results are shown in Figure 7.

Alternation between CAConv and RAConv with lazy-SISO results in  $1.23\times$  speedup, and HP  $1.75\times$  additional speedup in CPU. HP is also effective in GPU, inducing  $1.69\times$  speedup of computation. Meanwhile, image slicing results in  $1.67\times$  latency reduction in GPU, but leads to a slight slowdown ( $2.5\%$ ) in CPU due to the added computation of plaintext permutation. The memory capacity of our CPU system is large enough to accommodate the whole working set for all cases (see Table III). Therefore, although image slicing is able to save hundreds of GBs of memory space by reducing the aggregate size of

TABLE IV: HyPHEN Inference time of a single CIFAR-10 image using ResNet20/32/44 and a single ImageNet image using ResNet18 on CPU and GPU. As FC and pooling layers have a tiny execution time, we gather them at Others. For ResNet18, we implement stem convolution by im2col, which are also summed in Others.

Execution time (s)	CPU (64 threads)				GPU			
	ResNet20	ResNet32	ResNet44	ResNet18	ResNet20	ResNet32	ResNet44	ResNet18
<b>HP-CAConv</b>	12.85	19.39	24.42	160.86	0.46	0.66	0.87	6.27
<b>HP-RAConv</b>	1.68	3.02	4.01	36.45	0.06	0.09	0.13	3.35
<b>Bootstrap</b>	21.40	34.23	45.90	134.62	0.83	1.32	1.83	5.36
<b>Activation</b>	1.41	2.41	3.27	10.51	0.05	0.09	0.12	0.37
<b>Others</b>	0.23	0.30	0.44	43.86	<0.01	<0.01	0.01	1.52
<b>Total</b>	$37.57 \pm 0.7$	$59.35 \pm 0.9$	$78.04 \pm 0.8$	$386.30 \pm 5.4$	$1.40 \pm 0.04$	$2.17 \pm 0.04$	$2.96 \pm 0.04$	$16.87 \pm 0.08$

TABLE V: Comparison of the unencrypted inference accuracy (Backbone) and HCNN inference accuracy (HyPHEN) of the ResNet models for CIFAR-10.

Top-1 Acc (%)	ResNet20	ResNet32	ResNet44
<b>Backbone</b>	92.18	93.36	94.04
<b>HyPHEN</b>	92.17	93.35	94.08

weight plaintexts by roughly  $s_i = 8$  times, it does not lead to reduction in latency for our CPU system. However, for the GPU system, image slicing enables the whole working set to fit in the 80GB GPU memory, so also reduces the latency by removing the runtime overhead of copying data from the host to the GPU (Memcpy). Overall, image slicing has benefits of substantial memory footprint reduction and also latency reduction for memory-constrained systems.

#### D. Execution Time Breakdown

Table IV shows the runtimes of ResNet20/32/44 for the inference of a single CIFAR-10 image and ResNet18 for a single ImageNet image. Our ResNet20/32/44 implementations on GPU take merely a few seconds to complete. While the majority of inference time for ResNet20/32/44 is spent on bootstrapping, for ResNet18, 51.1% to 57.0% of inference time is spent on convolution as ResNet18 has four times more channels than ResNet20/32/44. Table IV also demonstrates that RAConv effectively reduces the overall runtime of the convolution layers, following the operation count analysis in Table VIII. We provide more detailed comparison with [11] in Appendix A.

#### E. Accuracy

In Table V, we measured inference accuracies for CIFAR-10 running ResNet models with HyPHEN.<sup>1</sup> Near-zero accuracy degradation ( $\leq 0.01\%$ ) is observed for ResNet20/32/44. HyPHEN is more robust to accuracy degradation than [11], which shows 0.09% to 0.21% accuracy degradation for ResNet20/32/44 on CIFAR-10. The difference in accuracy drop can be explained by whether the original network is executed

<sup>1</sup>We are still experimenting on the ImageNet accuracy, and will report the accuracy of the ResNet18 model for ImageNet in the revised version.

as is (using AESPA) or an approximation has been made (using ReLU approximation).

#### V. FUTURE WORK

We have shown the effectiveness of HyPHEN on HCNN using ResNet as representative CNN models. Exploring application of HyPHEN to a broader scope, such as application to various models as in [37], is needed as future work.

#### VI. CONCLUSION

In this paper, we proposed HyPHEN, an efficient private inference construction of FHE-based CNN (HCNN). Mixing two convolution methods with lazy-SISO and hybrid packing (HP) enables fast inference by significantly reducing the number of homomorphic rotations in convolution. Also, image slicing enables HyPHEN to reduce the memory footprint for high resolution image classification tasks, which is especially beneficial for memory-constrained devices. Our experiments with HyPHEN on CPU systems show  $1.87\times$  lower latency compared to the prior state-of-the-art implementation. Using GPU acceleration, HyPHEN achieves 1.40s/2.17s/2.96s execution time for running ResNet20/32/44 for CIFAR-10, and we also showed HCNN inference of ResNet18 for ImageNet in 16.87s for the first time.

#### REFERENCES

- [1] EU, "Regulation (eu) 2016/679 of the european parliament and of the council," 2016. [Online]. Available: <http://data.europa.eu/eli/reg/2016/679/oj>
- [2] U.S. Department of Health & Human Services, "Health insurance portability and accountability act of 1996," 1996. [Online]. Available: <https://www.hhs.gov/hipaa/index.html>
- [3] N. Kumar, M. Rathee, N. Chandran, D. Gupta, A. Rastogi, and R. Sharma, "Cryptflow: Secure tensorflow inference," in *2020 IEEE Symposium on Security and Privacy, SP 2020, San Francisco, CA, USA, May 18-21, 2020*, 2020. [Online]. Available: <https://doi.org/10.1109/SP40000.2020.00092>
- [4] W. Bowditch, W. Abramson, W. J. Buchanan, N. Pitropakis, and A. J. Hall, "Privacy-preserving surveillance methods using homomorphic encryption," in *Proceedings of the 6th International Conference on Information Systems Security and Privacy, ICISSP 2020, Valletta, Malta, February 25-27, 2020*. SCITEPRESS, 2020. [Online]. Available: <https://doi.org/10.5220/0008864902400248>
- [5] C. Gentry, "Fully homomorphic encryption using ideal lattices," in *Proceedings of the 41st Annual ACM Symposium on Theory of Computing, STOC 2009, Bethesda, MD, USA, May 31 - June 2, 2009*, 2009. [Online]. Available: <https://doi.org/10.1145/1536414.1536440>

- [6] A. C. Yao, "Protocols for secure computations (extended abstract)," in *23rd Annual Symposium on Foundations of Computer Science, Chicago, Illinois, USA, 3-5 November 1982*. IEEE Computer Society, 1982. [Online]. Available: <https://doi.org/10.1109/SFCS.1982.38>
- [7] V. Costan and S. Devadas, "Intel SGX Explained," *IACR Cryptol. ePrint Arch.*, 2016. [Online]. Available: <http://eprint.iacr.org/2016/086>
- [8] R. Gilad-Bachrach, N. Dowlin, K. Laine, K. E. Lauter, M. Naehrig, and J. Wernsing, "Cryptonets: Applying neural networks to encrypted data with high throughput and accuracy," in *Proceedings of the 33rd International Conference on Machine Learning, ICML 2016, New York City, NY, USA, June 19-24, 2016*, vol. 48, 2016. [Online]. Available: <http://proceedings.mlr.press/v48/gilad-bachrach16.html>
- [9] A. Brutzkus, R. Gilad-Bachrach, and O. Elisha, "Low latency privacy preserving inference," in *Proceedings of the 36th International Conference on Machine Learning, ICML 2019, 9-15 June 2019, Long Beach, California, USA, 2019*. [Online]. Available: <http://proceedings.mlr.press/v97/brutzkus19a.html>
- [10] R. Dathathri, B. Kostova, O. Saarikivi, W. Dai, K. Laine, and M. Musuvathi, "EVA: an encrypted vector arithmetic language and compiler for efficient homomorphic computation," in *Proceedings of the 41st ACM SIGPLAN International Conference on Programming Language Design and Implementation, PLDI 2020, London, UK, June 15-20, 2020*, 2020. [Online]. Available: <https://doi.org/10.1145/3385412.3386023>
- [11] E. Lee, J. Lee, J. Lee, Y. Kim, Y. Kim, J. No, and W. Choi, "Low-complexity deep convolutional neural networks on fully homomorphic encryption using multiplexed parallel convolutions," in *International Conference on Machine Learning, ICML 2022, 17-23 July 2022, Baltimore, Maryland, USA, 2022*. [Online]. Available: <https://proceedings.mlr.press/v162/lee22e.html>
- [12] E. Aharoni, A. Adir, M. Baruch, N. Drucker, G. Ezov, A. Farkash, L. Greenberg, R. Masalha, G. Moshkovich, D. Murik *et al.*, "Helayers: A tile tensors framework for large neural networks on encrypted data," *arXiv e-prints*, pp. arXiv-2011, 2020.
- [13] J.-W. Lee, H. Kang, Y. Lee, W. Choi, J. Eom, M. Deryabin, E. Lee, J. Lee, D. Yoo, Y.-S. Kim, and J.-S. No, "Privacy-preserving machine learning with fully homomorphic encryption for deep neural network," *IEEE Access*, vol. 10, pp. 30039-30054, 2022. [Online]. Available: <https://doi.org/10.1109/ACCESS.2022.3159694>
- [14] C. Juvekar, V. Vaikuntanathan, and A. P. Chandrakasan, "GAZELLE: A low latency framework for secure neural network inference," in *27th USENIX Security Symposium, USENIX Security 2018, Baltimore, MD, USA, August 15-17, 2018*, 2018. [Online]. Available: <https://www.usenix.org/conference/usenixsecurity18/presentation/juvekar>
- [15] D. Rathee, M. Rathee, N. Kumar, N. Chandran, D. Gupta, A. Rastogi, and R. Sharma, "Cryptflow2: Practical 2-party secure inference," in *CCS '20: 2020 ACM SIGSAC Conference on Computer and Communications Security, Virtual Event, USA, November 9-13, 2020*, 2020. [Online]. Available: <https://doi.org/10.1145/3372297.3417274>
- [16] Q. Zhang, C. Xin, and H. Wu, "GALA: greedy computation for linear algebra in privacy-preserved neural networks," in *28th Annual Network and Distributed System Security Symposium, NDSS 2021, virtually, February 21-25, 2021*, 2021.
- [17] P. Mishra, R. Lehmkuhl, A. Srinivasan, W. Zheng, and R. A. Popa, "Delphi: A cryptographic inference service for neural networks," in *29th USENIX Security Symposium, USENIX Security 2020, August 12-14, 2020*, 2020. [Online]. Available: <https://www.usenix.org/conference/usenixsecurity20/presentation/mishra>
- [18] Z. Huang, W. Lu, C. Hong, and J. Ding, "Cheetah: Lean and fast secure two-party deep neural network inference," in *31st USENIX Security Symposium, USENIX Security 2022, Boston, MA, USA, August 10-12, 2022*, K. R. B. Butler and K. Thomas, Eds., 2022. [Online]. Available: <https://www.usenix.org/conference/usenixsecurity22/presentation/huang-zhicong>
- [19] J. H. Cheon, K. Han, A. Kim, M. Kim, and Y. Song, "A full RNS variant of approximate homomorphic encryption," in *Selected Areas in Cryptography - SAC 2018 - 25th International Conference, Calgary, AB, Canada, August 15-17, 2018, Revised Selected Papers*, 2018. [Online]. Available: [https://doi.org/10.1007/978-3-030-10970-7\\_16](https://doi.org/10.1007/978-3-030-10970-7_16)
- [20] J. Bossuat, J. R. Troncoso-Pastoriza, and J. Hubaux, "Bootstrapping for approximate homomorphic encryption with negligible failure-probability by using sparse-secret encapsulation," in *Applied Cryptography and Network Security - 20th International Conference, ACNS 2022, Rome, Italy, June 20-23, 2022, Proceedings*, 2022. [Online]. Available: [https://doi.org/10.1007/978-3-031-09234-3\\_26](https://doi.org/10.1007/978-3-031-09234-3_26)
- [21] J. Bossuat, C. Mouchet, J. R. Troncoso-Pastoriza, and J. Hubaux, "Efficient bootstrapping for approximate homomorphic encryption with non-sparse keys," in *Advances in Cryptology - EUROCRYPT 2021 - 40th Annual International Conference on the Theory and Applications of Cryptographic Techniques, Zagreb, Croatia, October 17-21, 2021, Proceedings, Part I*, 2021. [Online]. Available: [https://doi.org/10.1007/978-3-030-77870-5\\_21](https://doi.org/10.1007/978-3-030-77870-5_21)
- [22] W. Jung, S. Kim, J. Ahn, J. H. Cheon, and Y. Lee, "Over 100x faster bootstrapping in fully homomorphic encryption through memory-centric optimization with gpus," *IACR Trans. Cryptogr. Hardw. Embed. Syst.*, 2021. [Online]. Available: <https://doi.org/10.46586/tches.v2021.i4.114-148>
- [23] Y. Lee, J. Lee, Y. Kim, Y. Kim, J. No, and H. Kang, "High-precision bootstrapping for approximate homomorphic encryption by error variance minimization," in *Advances in Cryptology - EUROCRYPT 2022 - 41st Annual International Conference on the Theory and Applications of Cryptographic Techniques, Trondheim, Norway, May 30 - June 3, 2022, Proceedings, Part I*, 2022. [Online]. Available: [https://doi.org/10.1007/978-3-031-06944-4\\_19](https://doi.org/10.1007/978-3-031-06944-4_19)
- [24] Q. Lou and L. Jiang, "HEMET: A homomorphic-encryption-friendly privacy-preserving mobile neural network architecture," in *Proceedings of the 38th International Conference on Machine Learning, ICML 2021, 18-24 July 2021, Virtual Event*, 2021. [Online]. Available: <http://proceedings.mlr.press/v139/lou21a.html>
- [25] J. Lee, E. Lee, J. Lee, Y. Kim, Y. Kim, and J. No, "Precise approximation of convolutional neural networks for homomorphically encrypted data," *CoRR*, vol. abs/2105.10879, 2021. [Online]. Available: <https://arxiv.org/abs/2105.10879>
- [26] T. Ishiyama, T. Suzuki, and H. Yamana, "Highly accurate CNN inference using approximate activation functions over homomorphic encryption," in *2020 IEEE International Conference on Big Data (IEEE BigData 2020), Atlanta, GA, USA, December 10-13, 2020*, 2020. [Online]. Available: <https://doi.org/10.1109/BigData50022.2020.9378372>
- [27] H. Chabanne, A. de Wargny, J. Milgram, C. Morel, and E. Prouff, "Privacy-preserving classification on deep neural network," *IACR Cryptol. ePrint Arch.*, 2017. [Online]. Available: <http://eprint.iacr.org/2017/035>
- [28] S. Obla, X. Gong, A. Aloufi, P. Hu, and D. Takabi, "Effective activation functions for homomorphic evaluation of deep neural networks," *IEEE Access*, vol. 8, 2020. [Online]. Available: <https://doi.org/10.1109/ACCESS.2020.3017436>
- [29] E. Hesamifard, H. Takabi, and M. Ghasemi, "Deep neural networks classification over encrypted data," in *Proceedings of the Ninth ACM Conference on Data and Application Security and Privacy, CODASPY 2019, Richardson, TX, USA, March 25-27, 2019*, 2019. [Online]. Available: <https://doi.org/10.1145/3292006.3300044>
- [30] P. Thaine, S. Gorbunov, and G. Penn, "Efficient evaluation of activation functions over encrypted data," in *2019 IEEE Security and Privacy Workshops, SP Workshops 2019, San Francisco, CA, USA, May 19-23, 2019*, 2019. [Online]. Available: <https://doi.org/10.1109/SPW.2019.00022>
- [31] J. Park, M. J. Kim, W. Jung, and J. Ahn, "AESPA: accuracy preserving low-degree polynomial activation for fast private inference," *CoRR*, 2022. [Online]. Available: <https://arxiv.org/abs/2201.06699>
- [32] K. He, X. Zhang, S. Ren, and J. Sun, "Deep residual learning for image recognition," in *2016 IEEE Conference on Computer Vision and Pattern Recognition, CVPR 2016, Las Vegas, NV, USA, June 27-30, 2016*, 2016. [Online]. Available: <https://doi.org/10.1109/CVPR.2016.90>
- [33] Crypto Lab, "HEEan library," 2022. [Online]. Available: <https://heean.it/>
- [34] A. Krizhevsky, G. Hinton *et al.*, "Learning multiple layers of features from tiny images," 2009.
- [35] O. Russakovsky, J. Deng, H. Su, J. Krause, S. Satheesh, S. Ma, Z. Huang, A. Karpathy, A. Khosla, M. S. Bernstein, A. C. Berg, and L. Fei-Fei, "Imagenet large scale visual recognition challenge," *Int. J. Comput. Vis.*, vol. 115, no. 3, 2015. [Online]. Available: <https://doi.org/10.1007/s11263-015-0816-y>
- [36] J. H. Cheon, M. Hhan, S. Hong, and Y. Son, "A hybrid of dual and meet-in-the-middle attack on sparse and ternary secret LWE," *IEEE Access*, 2019. [Online]. Available: <https://doi.org/10.1109/ACCESS.2019.2925425>
- [37] Z. Liu, H. Mao, C. Wu, C. Feichtenhofer, T. Darrell, and S. Xie, "A convnet for the 2020s," *CoRR*, vol. abs/2201.03545, 2022. [Online]. Available: <https://arxiv.org/abs/2201.03545>
- [38] A. Paszke, S. Gross, F. Massa, A. Lerer, J. Bradbury, G. Chanan, T. Killeen, Z. Lin, N. Gimelshein, L. Antiga, A. Desmaison, A. Kopf, E. Yang, Z. DeVito, M. Raison, A. Tejani, S. Chilamkurthy, B. Steiner, L. Fang, J. Bai, and S. Chintala, "Pytorch: An



- imperative style, high-performance deep learning library,” in *Advances in Neural Information Processing Systems 32*, 2019, pp. 8024–8035. [Online]. Available: <http://papers.neurips.cc/paper/9015-pytorch-an-imperative-style-high-performance-deep-learning-library.pdf>
- [39] G. E. Hinton, O. Vinyals, and J. Dean, “Distilling the knowledge in a neural network,” *CoRR*, 2015. [Online]. Available: <http://arxiv.org/abs/1503.02531>
- [40] K. Han and D. Ki, “Better bootstrapping for approximate homomorphic encryption,” *IACR Cryptol. ePrint Arch.*, 2019. [Online]. Available: <https://eprint.iacr.org/2019/688>

APPENDIX

Figure 8 shows the runtime analysis of the convolutional layers of ResNet20. In MP-CACConv [11], rotation accounts for 83-94% of the total convolution time, which is reduced to 46-77% with our method. Optimizations of HyPHEN lead to rotation taking a smaller portion of the execution latency. Table VI shows runtime breakdown of the ResNet models for CIFAR-10 and ImageNet, with detailed operation-by-operation comparison with [11] in our CPU environment. As we set both implementations to use AESPA with the same HE parameter set, the speedup is solely due to the algorithms and packing schemes. Latency improvements in convolution layers lead to  $1.82\times$  faster total execution time in ResNet20. In ImageNet classification using ResNet18, HyPHEN trades off rotations with bootstrapping operations reports as shown in Table VIII resulting increased runtime in activation function and bootstrapping time. However, It leads to  $2.09\times$  lower overall execution time.

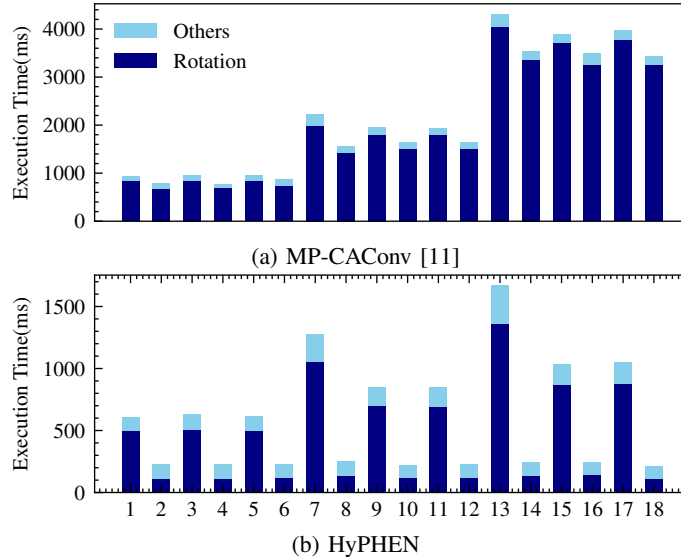


Fig. 8: Comparison of rotation time in ResNet20 convolutional layers

TABLE VI: HyPHEN inference time of a single image using ResNet models on CPU. As FC and pooling layers have a tiny execution time, we gather them at Others.

Execution time (s)	ResNet20 (CIFAR-10)				ResNet18 (ImageNet)			
	Ours		[11]		Ours		[11]	
	runtime	percent	runtime	percent	runtime	percent	runtime	percent
CACConv	12.84	34.2 %	47.17	68.8%	160.86	41.7%	690.41	85.4%
RACConv	1.68	4.5%	-	-	36.45	9.4%	-	-
Bootstrap	21.40	56.9%	20.86	30.4 %	134.62	34.8%	78.80	9.7%
Activation	1.41	3.7%	0.33	0.5%	10.51	2.7%	1.12	0.01 %
Others	0.22	0.6%	0.22	0.3%	43.86	11.4%	38.52	4.8 %
<b>Total</b>	37.57 ± 0.3 100%		68.58 ± 0.8 100%		386.30 ± 5.4 100%		808.85 ± 18.1 100%	

We present a parameter study to explore the optimal HP setting which minimizes latency. Table VII and show the rotation and bootstrapping counts with varying  $(m, d)$  available in ResNet20 and the execution time running the network on GPU. We only represent the  $(m, d)$  pair of CACConv, as  $m$  and  $d$  are exchanged at RACConv. In ResNet20, we start with  $(m, d) = (1, 2)$  to remove input repetition as the size of the input tensor in the first layer ( $32 \times 32 \times 16$ ) is smaller than the ciphertext slots ( $2^{15}$ ). Nevertheless, Larger  $d$  has not been considered as it leads to more bootstrapping, as shown in our proposed architecture (See Figure 6). As the input ciphertexts go through the downsampling layer,  $m \cdot d$  gets quadrupled and the size of the intermediate tensor gets halved. HP that doubles  $d$  every downsampling layer yields optimal performance, which reduces rotation without increasing bootstrap. In ResNet18, the impact of bootstrapping increment is often smaller than the impact of rotation decrement. The optimal HP setting requires 27 more bootstrappings and 20641 fewer rotations than the minimum bootstrapping HP setting.

Figure 9 presents model architecture of modified ResNet20 used in HCNN evaluation. Table IX and X shows parameters used in the convolution layers of ResNet20/32/44/18. All the parameters  $(c_i, c_o, w_i, h_i, w_o, h_o, f_w, f_h, s)$  are determined following the original ResNet paper [32].

Models used in this paper is all trained using PyTorch [38]. For ResNet18 and 20, our training settings are mostly identical to AESPA; specifically, networks are trained for 200 epochs using SGD optimizer, 0.1 initial learning rate, 100 batch size, 0.0005 weight decay and 0.9 momentum, and cosine annealing scheduler. We also use soft labels as in [31] to get higher accuracy. For ResNet32 and 44, we use knowledge distillation [39] to enhance the accuracy, using pre-trained ResNet32/44 with

TABLE VII: Comparison of the instances of CAConv (m,d) parameters in ResNet20.

L1	(m,d)		SISO	Rotations			total	Boot	GPU Runtime(s)
	L2	L3		RaS	IR				
(1,2)	(2,4)	(4,8)	152	580	187	919	11	1.40 ± 0.04	
(1,2)	(2,4)	(2,16)	192	539	162	893	13	1.54 ± 0.05	
(1,2)	(1,8)	(4,8)	200	448	165	813	14	1.56 ± 0.04	
(1,2)	(1,8)	(2,16)	240	407	142	789	16	1.66 ± 0.05	
(1,2)	(1,8)	(1,32)	240	419	154	831	20	2.04 ± 0.04	

TABLE VIII: Runtime for the ResNet instances with different (m, d) parameters and packing strategies.

Model	Packing	(m,d)				SISO	Rotations			Boot	CPU Runtime(s)
		L1	L2	L3	L4		RaS	IR	total		
ResNet20	MP-CAConv	(1,2)	(2,4)	(4,8)	-	152	924	800	1876	10	68.58 ± 1.0
	Optimal	(1,2)	(2,4)	(4,8)	-	152	580	187	919	10	37.57 ± 0.7
	Min Rot	(1,2)	(1,8)	(2,16)	-	240	407	142	789	16	44.51 ± 0.5
ResNet18	MP-CAConv	(1,1)	(4,1)	(16,1)	(64,1)	536	32384	4669	37589	38	808.86 ± 18.1
	Min Boot	(1,1)	(2,2)	(4,4)	(8,8)	536	17920	9544	28000	38	660.58 ± 11.6
	Optimal	(1,1)	(2,2)	(4,4)	(8,8)	1024	4512	1823	7359	65	377.02 ± 6.3

93.4% and 94.1% accuracies as teacher models. As the FC layer of the student and teacher network is identical, the teacher’s FC layer is directly reused in the student network. We trained the student networks by minimizing  $l_2$  loss ( $L_{kd} = \|f_t - f_s\|_2^2$ ). ResNet32 and 44 are trained for 240 epochs using SGD optimizer, 0.0005 weight decay and 0.9 momentum. We use 0.05 initial learning rate and learning rate scheduler decays the learning rate on epochs 150, 180, 210 by 0.1.

Unlike the original SISO convolution which rotates input ciphertexts before multiplying with filter plaintexts, lazy-SISO suspend rotation by multiplying intact input ciphertext with inversely rotated filter plaintexts. The actual process of lazy-SISO when  $c_i, c_o = 1$  is depicted in Figure 10. After multiplying with filter plaintext, postponed rotation is performed after accumulating intermediate ciphertexts. During this process, multiple ciphertexts sharing the same rotation index are grouped to be accumulated first and SISO rotation is conducted to reduced ciphertexts (e.g.,  $c_i$  ciphertexts are accumulated before rotation in Figure 2c). Lazy-SISO is beneficial when accumulated  $ct_{out}$  is smaller than  $ct_{in}$ , which often occurs in RAConv. Generally, We can select between SISO and lazy-SISO greedily to perform rotations on  $\min(ct_{in}, ct_{out})$  ciphertexts.

Memory requirement for HCNN depends on FHE parameters and data representations (packing schemes). In FHE, expansion of data size occurs while encryption and encoding procedures. Resulting ciphertexts and plaintexts are typically orders of magnitude larger than messages. Table XI shows the actual size of the ciphertext, plaintext and evaluation key on two FHE parameter settings. `dnum` denotes RNS-decomposition number introduced in [40]. Given  $N$ , the degree of a cyclotomic polynomial ring, large `dnum` increases  $L$ , max level. `ParamSet1` is a setting used in [11]. As [11] approximates ReLU with high degree polynomial for activation, `ParamSet1` adopts maximum `dnum` to have  $L' = 16$ . `ParamSet2` is the parameter set used in this work. AESPA enables us to select light RNS-CKKS parameter ( $L' = 6$ ), as activation consumes one level. Some FHE operations such as `MulCt`, `Rotate` and `Conjugate` requires the key switching procedure. `Eval key` denotes public key used during this process. The size of a single `Eval key` is 2,147MB and 176MB in `ParamSet1` and `ParamSet2`, respectively. To support bootstrapping, one relinearization key for `MulCt`, one conjugation key and 48 rotation keys are required. We additionally load frequently used rotation keys to perform convolution. For instance, We load 64 unique `Eval keys` in ResNet18 which take up 137.4GB and 11.3GB in `ParamSet1` and `ParamSet2`, respectively.

Once FHE parameter is determined, the packing scheme determines the number of ciphertexts and plaintexts to run each ResNet block. Table XII and Table XIII show the required number and total memory size of ciphertexts and plaintexts. We further explain the actual computation procedure to explain how the results are obtained in Appendix A. In SISO-based HCNN kernel, the size of filter plaintexts increases by a factor of  $w_i h_i$  as each filter element is duplicated to the size of input image, which requires a total of  $f_w f_h w_i h_i c_i c_o$  slots for weight plaintexts. In consequence, weight plaintexts take up the majority of memory regardless of the ciphertext packing method. In Table XII, our implementation shows up to 14.75% memory overhead compared to [11], which is primarily due to the increase in the number of ciphertexts and bias plaintexts. In Table XIII, our implementation shows up to 6.04-6.58× memory reduction compared to [11].

In this section, we describe implementation details about the ResNet18 model on the ImageNet dataset. The runtime is 16.87 seconds in our GPU environment. As shown in Figure 11, the network receives input ciphertexts processed with modified `im2col`. Original `im2col` would transform  $224 \times 224 \times 3$  images into  $147 \times 12544$  matrices. As HCNN prefers image size to be exponential of 2, 12544 columns turns to 16384 columns. We further split 16384 columns with stride 2 ( $s_{avg}$  in Figure 11) to perform average pooling without rotation, resulting in 4096 columns. We pack  $slot/4096 = 8$  rows in a ciphertext. As the total number of rows is  $f_h f_w c_i = 147$ , the number of input ciphertext is  $\lceil 147/8 \rceil \times 4$ . After the initial convolution layer, the number of intermediate ciphertexts becomes 64 and each ciphertext stores 8 channels with (m,d) = 1.

Figure 12 and Figure 13 show the complete procedure of CAConv and RAConv with HP, previously shown briefly in Figure 4. Both CAConv and RAConv perform a sequence of  $\{SISO, RaS, IR\}$  to the input ciphertexts. As in Figure 2, a

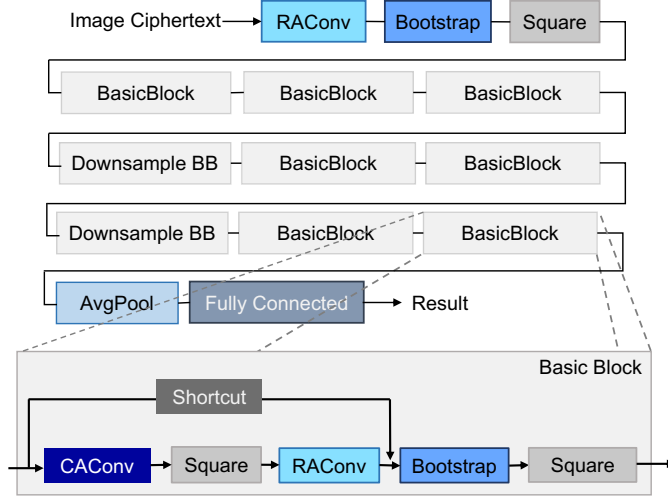


Fig. 9: The ResNet20 structure of HyPHEN.

TABLE IX: Parameters used in the convolution layers of ResNet20/32/44

	Layer1	Layer2			Layer3		
	conv	dsconv	pconv	conv	dsconv	pconv	conv
$c_i$	16	16	16	32	32	32	64
$c_o$	16	32	32	32	64	64	64
$w_i (= h_i)$	32	32	32	16	16	16	8
$w_o (= h_o)$	32	16	16	16	8	8	8
$f_w (= f_h)$	3	3	1	3	3	1	3
$s$	1	2	2	1	2	2	1

single superscript represents the channel of input images, and a superscript pair represents (input channel, output channel) of filters. If multiple channels are stored in a box, we represent the list of channels using  $\&$  or the range of channels using  $-$ . We set  $c_i, c_o = 32$  and  $w_i, h_i = 16$  following the second layer of ResNet20. In HP-CAConv (Figure 12), the HP setting of input ciphertext is  $(m, d) = (2, 4)$ . In HP-RAConv (Figure 13), the HP setting of input ciphertext is  $(m, d) = (4, 2)$ .

We use different brightness of color to fill the ciphertexts and plaintexts to reflect the actual computation process. In Figure 12 and Figure 13, the intermediate ciphertexts of the CAConv and input ciphertexts of the RAConv are  $\frac{c_o}{4}$  and  $\frac{c_i}{4}$  times larger than the input ciphertext of CAConv, respectively. CAConv, activation and RAConv in a ResNet block is processed at once to mitigate the huge number of intermediate ciphertexts. To avoid an increase of the memory footprint, operations on the input ciphertext continues until the ciphertext shrinks again. Thus, the tuple of operations  $\{SISO, RaS, IR, Square, SISO_i\}$  are processed to an input ciphertext and then accumulated. Blocks colored with high brightness show actual working set, which means  $\frac{c_o}{4}$  times larger intermediate ciphertexts (colored with low brightness) are irrelevant with the peak memory consumption.

TABLE X: Parameters used in the convolution layers of ResNet18

	Layer1	Layer2			Layer3			Layer4		
	conv	dsconv	pconv	conv	dsconv	pconv	conv	dsconv	pconv	conv
$c_i$	64	64	64	128	128	128	256	256	256	512
$c_o$	64	128	128	128	256	256	256	512	512	512
$w_i (= h_i)$	32	32	32	16	16	8	8	8	4	4
$w_o (= h_o)$	32	16	16	16	8	8	8	4	4	4
$f_w (= f_h)$	3	3	1	3	3	1	3	3	1	3
$s$	1	2	2	1	2	2	1	2	2	1

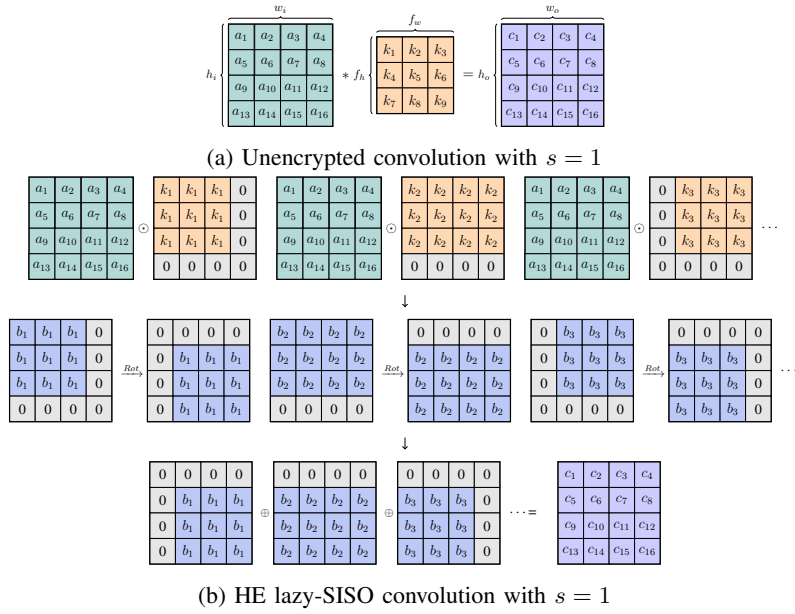


Fig. 10: Lazy-SISO convolution.

TABLE XI: FHE parameter settings.  $d_{num}$  is tuned to support 16, 6 levels required in  $Set1$ , and  $Set2$ . Each ciphertext and plaintext memory size is represented when current level  $l = L'$ .

	L	L'	$d_{num}$	Ciphertext (MB)	Plaintext (MB)	Eval Key (MB)	Total Keys(GB)
ParamSet1	32	16	32	17.82	8.91	2,147.48	137.44
ParamSet2	24	6	6	10.48	5.24	176.16	11.27

TABLE XII: Total memory size and the number of each object in ResNet20. We abbreviated Downsampling Block and Basic Block to DSB and BB.

ResNet20	Layer1 BB		Layer2				Layer3			
	Ours	Lee	DSB	Lee	BB	Lee	DSB	Lee	BB	Lee
filter ptxts	144	144	232	232	144	144	232	232	144	144
input cxtxs	1	1	1	1	1	1	1	1	1	1
peak cxtxs	19	10	19	10	19	10	19	10	19	10
total size (GB)	0.70	0.68	1.18	1.07	0.79	0.69	1.19	1.08	0.79	0.71
memory overhead	0.3%		10.5%		14.7%		10.1%		12.0%	

TABLE XIII: Total memory size and the number of each object in ResNet18. DSB and BB refers to downsampling Block and basic block.

ResNet18	Layer1 BB		Layer2				Layer3				Layer4			
	Ours	Lee	DSB	Lee	BB	Lee	DSB	Lee	BB	Lee	DSB	Lee	BB	Lee
filter ptxts	1152	9216	1856	14848	1152	9216	1856	9216	1152	9216	1856	14848	1152	9216
input cxtxs	8	8	8	8	8	4	8	4	8	2	8	2	8	1
max cxtxs	137	73	137	73	137	37	137	37	137	19	137	19	137	10
total size (GB)	6.02	37.06	9.41	61.93	6.02	36.63	9.41	61.59	6.02	36.44	9.41	61.42	6.02	36.34
memory reduction	6.15×		6.58×		6.08×		6.55×		6.05×		6.53×		6.04×	

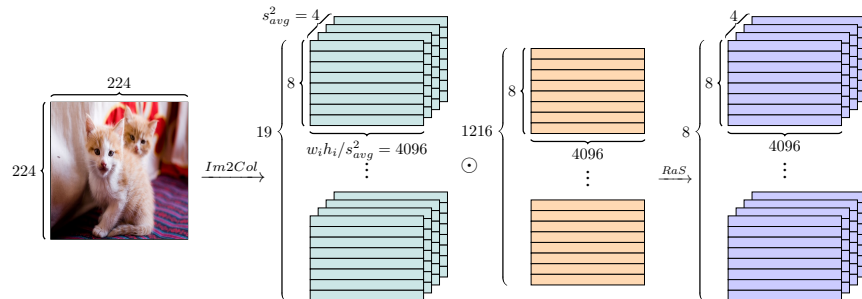


Fig. 11: ImageNet Im2Col

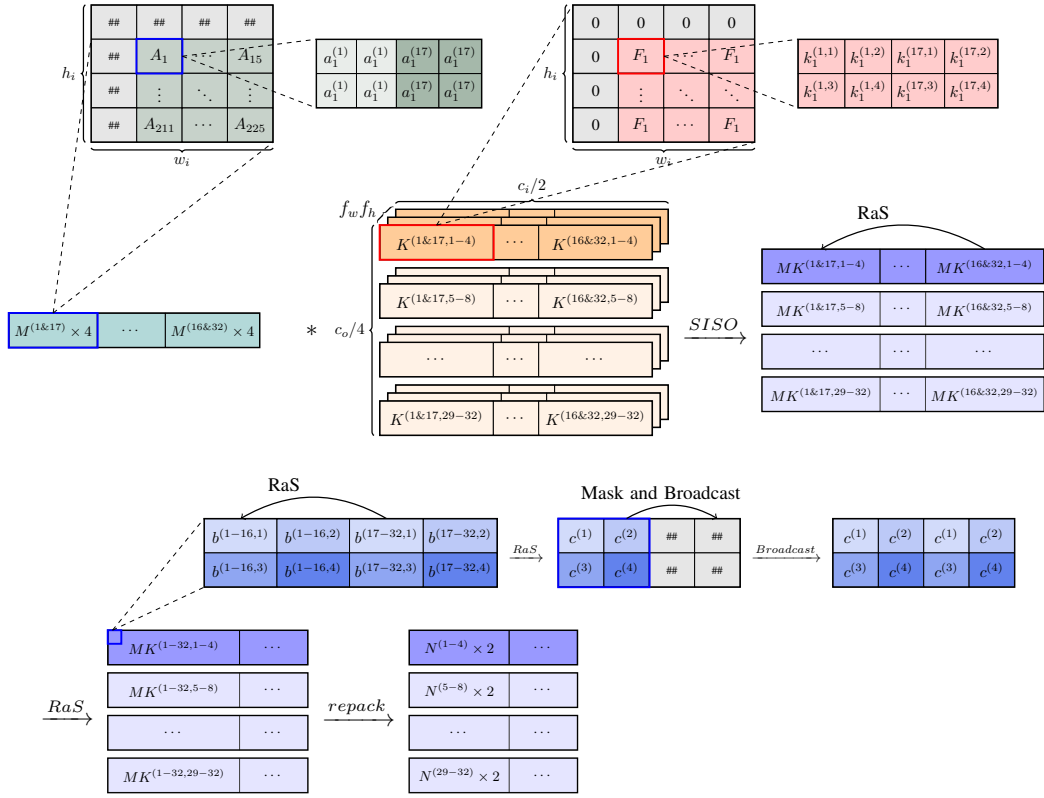


Fig. 12: CAConv method with HP

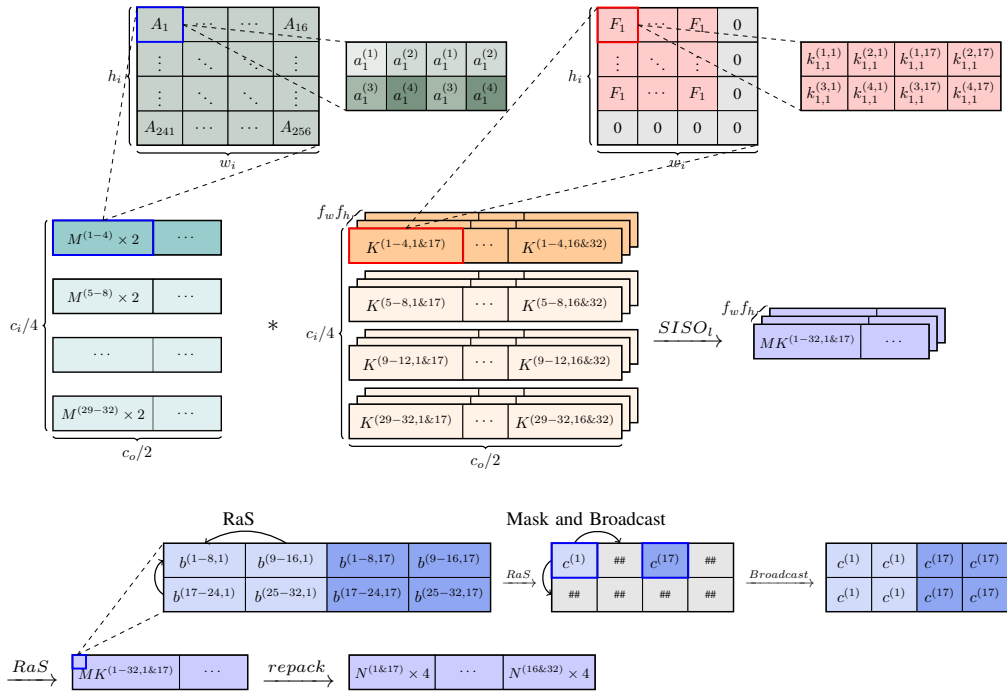


Fig. 13: RAConv method with HP